ACS APPLIED MATERIALS & INTERFACES

www.acsami.org

Research Article

Back-Reflected Performance-Enhanced Flexible Perovskite Photodetectors through Substrate Texturing with Femtosecond Laser

Ye Wang, Wenwei Liu, Wei Xin,* Tingting Zou, Xin Zheng, Yanshuang Li, Xiuhua Xie, Xiaojuan Sun, Weili Yu, Zhibo Liu, Shuqi Chen,* Jianjun Yang,* and Chunlei Guo*

Cite This: *ACS Appl. Mater. Interfaces* 2020, 12, 26614−26623

Read Online

ACCESS | Metrics & More | Article Recommendations | Supporting Information

ABSTRACT: Recently, enhancing the performance of flexible perovskite photodetectors through facile and effective means has gained greater attention. In contrast to typical approaches through modifying light-active materials, we present here a simple but effective design by improving light−matter interactions through near-field optical interference on a back-reflected substrate, whose architecture includes a morphologically flat top surface and a backscattering surface textured with micro/nanostructures by the femtosecond laser direct writing. A $CH_3NH_3PbI_3$ perovskite film and poly(ethylene terephthalate) are selected as the light-active and base materials, respectively. Under a 1 V bias voltage actuation and 532 nm laser irradiation at an intensity of 10 mW cm^{-2}, the flexible device exhibits excellent performance in photoresponsivity (47.1 mA W^{-1}), detectivity (3.7×10^{11} Jones), and on/off ratio (4600). Due to the near-field optical enhancement of the substrate and the strong light−matter interaction, the above performance parameters are enhanced by at least 5 times over a wide spectral range of 220−780 nm. Such enhancement behaviors are independent of active material properties and therefore can be compatible with other operations such as crystalline transformation, doping, and interface modification. Moreover, the alteration of stress distribution on the structured substrate facilitates the bending robustness and stability. These features highlight the potential of back-reflected design in the development of flexible perovskite photoelectric devices, which are especially suitable for large-scale industrial production.

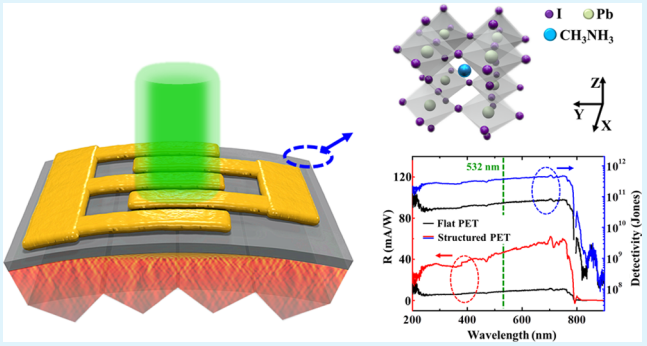

KEYWORDS: *flexible perovskite photodetector, back-reflected structure, performance enhancement, near-field optical interference, femtosecond laser engineering*

INTRODUCTION

Flexible photodetectors (FPDs) attract much attention in the field of optoelectronics in recent decades due to their excellent photoelectric and mechanical properties, which can meet the requirements of next-generation integrated devices for compatibility, portability, and simple and low-cost manufacturing.[1,2] To date, great efforts have been devoted to improve the performance of FPDs, which mainly focus on two aspects, i.e., optimizing the properties of light-active materials or modifying the way light interacts with matter. The former operation has been proved valid, which is usually achieved through interface modification, doping, or crystalline morphology transformation, but usually lacks flexibility, simplicity, or universality in terms of the performance enhancement of devices.[3−5] As a typical example, in 2012, Koppens's group improved the photoresponsivity (R) of the traditional graphene photodetector by 9 orders by suggesting a hybrid graphene−PbS quantum dot film as light-active material, but seriously sacrificed the wide spectral response characteristics of graphene.[6] By contrast, it is easy to implement and has been confirmed practical by modifying the light−matter interaction via different ideas, such as inserting materials into the Fabry−Perot microcavity for multiple light absorption, combining materials with plasmonic structures on substrates, and enhancing the evanescent wave effect at the material−substrate interface.[7−9] As one of the methods, introducing the micro/nanostructures with random or periodic morphologies on substrates of the samples has been extensively studied recently.[10−12] In this way, we can effectively change the optical field distribution and control the transmission of

Received: March 8, 2020
Accepted: May 18, 2020
Published: May 18, 2020

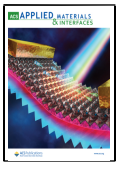

https://dx.doi.org/10.1021/acsami.0c04124
ACS Appl. Mater. Interfaces 2020, 12, 26614−26623

Table 1. Performance Comparison of Enhanced Perovskite-Based Photodetectors[a]

material structure	device type	response range (nm)	light wavelength (nm)/ power	bias (V)	on/off ratio	R (mA W^{-1})	D^* (Jones)	t_r/t_d (ms)	enhanced performance	motivator	refs
$MAPbI_3$/graphene (G)	phototransistor	400–800	520/1 × 10^{-3} mW	0.1		1.8 × 10^5	10^9	87/540	R	I	29
$MAPbI_3/WS_2$	photoconductor	470–620	505/0.5 mW cm^{-2}	5	10^4	1.7 × 10^4		2.7/7.5	D^*, t_r/t_d (4 orders)	I	30
$MAPbI_3$/ZnO nanowire (NW)	photoconductor	380–760	380/4.23 mW cm^{-2}	1		4 × 10^3	1.74 × 10^9	420/630	R (7.7 times)	I	31
$MAPbBr_2I$ island/G	phototransistor	405–633	405/1 nW	3		6 × 10^8		<120/750	R (4 orders)	I	32
$MAPbI_3$ island/G/ Au NPs	phototransistor	532	532/1.4 × 10^{-2} mW cm^{-2}	10		2.1 × 10^6		1800/1500	R	I	33
$MAPbI_{3-x}Cl_x$/ nanogold	photoconductor	405–850	655/5.7 pW	50	~10^5	2841	2.1 × 10^{13}	271/169	R (3 times), low detection limit (5.7 pW)	I	34
$MAPbI_3$/rGO	photoconductor	520	520/3.2 mW cm^{-2}	5	168	73.9		40.9/28.8	on/off ratio (6 orders), t_r/t_d	II	35
$MAPbICl_2$/ZnO nanofiber	photoconductor	380–730	730/100 mW cm^{-2}	1	22.56	6.7 × 10^2	1.4 × 10^{13}	~200/500	t_r/t_d, D^*, R (~20 times)	II	36
$MAPbI_3$/C8BTBT	photoconductor	365–808	532/7.5 μW cm^{-2}	3	9750	8.1 × 10^3	2.2 × 10^{12}	7100/6500	R	II	37
$MAPbI_3/NaYF_4$:Yb/ Er NPs	photoconductor	400–1000	980	2	>1000	270	7.6 × 10^{11}	52/67	D^* (3 times)	II	38
$MAPbI_3$/PDPP3T	photoconductor	365–937	835/5 μW cm^{-2}	1		1.54	8.8 × 10^{10}		R (8 times), response range	II	39
$MAPbI_3$ nanosheet	photoconductor	405–532	405/~1 pW	1	~100	2.2 × 10^4		<20/40	R -(~7 times)	III	40
$MAPbI_3$	photoconductor	400–800	680/42.5 μW cm^{-2}	1	~100	8.1 × 10^4	>10^{11}	0.38/0.23	R (3 orders)	III	28
$MAPbI_3$ NW	photoconductor	532	532/1 mW cm^{-2}	3	~13			~120/210	on/off ratio (1.2 times)	III	41
$MAPbI_3$ microarrays	photoconductor	560	560/22.9 mW cm^{-2}	2	1 × 10^3	480	1.3 × 10^{12}	36/43	R/D^*/EQE (~1 order)	III	42
$(C_4H_9NH_3)_2PbBr_4$ NWs/belts	photoconductor	365–405	365/318 mW cm^{-2}	5	46	1.1 × 10^{-2}		490/530	on/off ratio, R	III	43
$MAPbI_3$/Si nanoporous pillar arry	photodiode	400–1050	780/52.6 mW cm^{-2}	0	8.2 × 10^4	8.13	9.74 × 10^{12}	~0.25/0.23	on/off ratio; R; D^*;t_r/t_d	IV	25
$CsPbBr_3$/CNTs	photoconductor	vis	532/8.85 mW	3	>1 × 10^4	20	3 × 10^8	52/14	on/off ratio; t_r/t_d	IV	26
$MAPbI_3$/PTAA	photoconductor	600–900	800/1 mW cm^{-2}	1	~8		~7.1 × 10^{11}	<60	R/D^*/EQE (~9 times)	IV	44
$MAPbI_3$	photoconductor	200–780	532/10 mW cm^{-2}	1	4600	14.5	1.9 × 10^{11}	380/420	on/off ratio, R, D^*, (respective ~5.8, 5.8, 5.9 times), bending robustness	IV	our work

[a]The statements of interface modification, multicomposition doping, and crystalline morphology transformation are simplified as roman numerals I, II, and III, respectively. The statement of light–matter interaction alteration based on substrate treatment is simplified as IV.

https://dx.doi.org/10.1021/acsami.0c04124
ACS Appl. Mater. Interfaces 2020, 12, 26614–26623

photons. Since this operation only affects the way of light−matter interaction without changing the nature of the material itself, it shows material compatibility and complementarity. As a result, it is necessary to perform an in-depth study of this facile and effective light−matter interaction through substrate modulation, which is of great significance for the full use of materials in practical applications.

Here, we demonstrated a method that utilizes the periodic micro/nanostructures on a flexible substrate to achieve the near-field optical enhancement, thereby enhancing the photoresponse of light-active materials. We chose the structured poly(ethylene terephthalate) (PET) and perovskite film as the research objects, corresponding to the substrate and light-active material. The femtosecond laser direct writing (FsLDW) technology was used for the structure fabrication on the substrate. Compared to other manufacturing methods, such as hot embossing or electron beam lithography, the FsLDW technology shows superiority in terms of cost-effectiveness, efficiency, flexibility, and versatility.[13,14] Through laser processing, we created a periodic micron-sized sawtooth-shaped grating structure with tunable width and depth. The finite-difference time-domain (FDTD) method was also used to profile the near-field electric field distribution of the substrate before and after the processing.[15] Thanks to the larger refractive index (RI) and lower light absorption of PET in the UV−NIR spectral range, we demonstrated hundreds of orders of diffraction modes leading to the strong interference of electric fields especially in the areas near the substrate surface, contributing the basic element of strong light−matter interactions. Moreover, the laser melting and ablation also induced abundant hierarchical micro/nanostructures on the surface during the processing, which enhances the surface-to-volume ratio and probabilities of light scattering and trapping, further facilitating the light absorption of light-active materials.[12,16,17]

As for numerous perovskite materials employed in FPDs, $CH_3NH_3PbI_3$ ($MAPbI_3$) was often chosen for the research because it has been widely studied as an ideal building block due to its unique properties, such as large light absorption coefficients (~10^5 cm^{-1}), high power conversion efficiency (25.2%), wide spectral response (UV−vis), high carrier mobility (~800 cm^2 V^{-1} s^{-1}), small exciton-binding energy (<10 meV), and long electron−hole diffusion length (~0.1 to 10 μm).[18−24] Unlike most experiments, here, we deposited the $MAPbI_3$ film as thin as ~200 nm on the flat surface rather than on the structured back side of the substrate for light harvesting.[25,26] Such a thin film and the back-reflected type of construction make it possible to avoid the recycling and out-coupling phenomena of photons caused by the increased carrier leakage pathways of the hierarchical micro/nanostructures, effectively minimizing the impact of the defects on the photogenerated carrier recombination.[27,28]

Based on the above design, combining a PET substrate with the textured back surface and an $MAPbI_3$ film spun on its flat surface, we reported the fabrication of a back-reflected flexible perovskite photodetector with a more than 5-fold enhancement of photoresponsivity (~47.1 mA W^{-1}), detectivity (~3.7×10^{11} Jones), and on/off ratio (~4600) in the UV−vis region (220−780 nm). The increased external quantum efficiency (EQE) of the perovskite film caused by the structured substrate may play a key role.[17] Further material characterizations indicate that our method gives no change in the nature of materials and thus shows potential compatibility with other material modifications for further performance improvement.[29−31] Meanwhile, the laser processing also changes the overall stress distribution of the substrate, enhancing the robustness of the perovskite film with less fracture. Nearly 90% of the current intensity can still be maintained even after a small bending curvature (~4 mm) and 500 bending cycles. In the encapsulation of poly(methyl methacrylate) (PMMA), there was also no obvious degradation of the performance in air for more than 2 months. To illustrate the superior characteristics of our method in terms of the optoelectronic performance enhancement, a detailed comparison is summarized in Table 1.[25,26,28−44] By comparison, our design of the perovskite FPD is competitive in both optoelectronic and mechanical properties, indicating great potential for development in practical applications.

EXPERIMENTAL SECTION

Materials. All chemicals were purchased commercially and used as received. The $MAPbI_3$ precursor solution was synthesized by mixing MAI and lead iodide (PbI_2) at a 1:1 (0.162:0.462 g) equimolar ratio in *N*,*N*-dimethylformamide (DMF, 0.7 mL) and dimethyl sulfoxide (DMSO, 0.3 mL) at 70 °C and stirring for 6 h inside a nitrogen-filled glovebox.

Device Fabrication. Flexible substrates were processed by single-beam femtosecond laser pulses and then washed with ethanol, followed by nitrogen drying. After treatment in O_2 plasma (SAOT YZD08-2C) for 2 min, the $MAPbI_3$ perovskite layer was deposited by spin-coating of the $MAPbI_3$ precursor solution first at a rate of 500 rpm for 5 s and then at 2000 rpm for 60 s in the glovebox. After a 20 s delay, 500 μL of chlorobenzene was quickly added during the spin-coating procedure. The substrates were then heated at 70 and 105 °C for 2 and 8 min, respectively. During the annealing process, the color of the $MAPbI_3$ film changed from light yellow to black, indicating that the octahedral structure was gradually formed at a high temperature during the evaporation of the DMF and DMSO solvents. Gold electrodes were thermally deposited onto the $MAPbI_3$ film in a vacuum chamber at a pressure of ~2×10^{-4} Pa through a shadow mask, with channel length and width of 1500 and 200 μm, respectively. Furthermore, to maintain the long-term stability of the FPDs in air, the PMMA coverage (3000 rpm, 30s) was applied.

Characterization. The confocal microscope image was obtained by a Keyence Laser Microscope (Keyence VK-X1000). The X-ray diffraction (XRD) pattern was measured with a diffractometer (Rigaku D/Max-2500) using Cu Kα radiation (λ = 1.54 Å). The current−voltage (I−V) characteristics were measured using a 4200A-SCS Parameter Analysis (Keithley) in the dark and under 532 nm laser illumination. Scanning electron microscopy (SEM) images were recorded on a Hitachi S4800. Time-resolved photoluminescence (TRPL) was measured using the time-correlated single photon counting system (PICOQUANT Ltd.) excited with a 532 nm laser. The absorption spectrum of the $MAPbI_3$ film on flexible substrates and the reflection of the structured substrates were recorded by a Cary 5000 UV−vis−NIR spectrophotometer (Agilent, DRA 2500 integrating sphere). Energy-dispersive X-ray spectroscopy (EDS) analysis was carried out by a scanning electron microscope (Phenom ProX). The spectral response was measured with a Stanford SR830 lock-in amplifier under monochromatic illumination at a chopping frequency of 180 Hz by a Stanford SR540 chopper. All measurements were performed under ambient conditions and at room temperature.

Simulation and Experiment Demonstration of the Bending Performance of PET. We simulated the first principal stress distribution in the PET layer using Comsol Multiphysics software. The width and depth of the sawtooth-shaped grating were also determined as 30 and 10 μm, respectively. The characteristic parameters such as density, Young's modulus, and Poisson's ratio of PET were set as 1.38 g cm^{-3}, 4000 MPa, and 0.338, respectively. A fixed constraint was employed on the left-hand side of the PET layer, and a force of 50 N was loaded on the right-hand side to realize bending of the PET substrate. Furthermore, the dependence of microstrain ($\mu\varepsilon$ = $(\Delta L/L) \times 10^{-6}$) of PET substrates on its bending curvature was

https://dx.doi.org/10.1021/acsami.0c04124
ACS Appl. Mater. Interfaces 2020, 12, 26614−26623

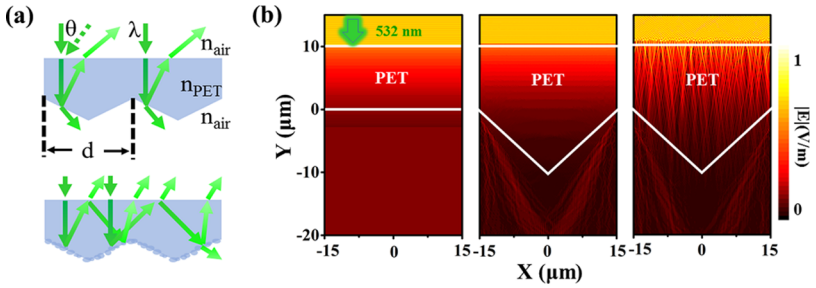

Figure 1. (a) Schematic of the ray tracing of light in the different structured PET substrates. The incident wavelength, incident angle, length of the structural unit, and the RI of air and PET are λ, θ, d, n_{air}, and n_{PET}, respectively. (b) Simulated near-field electric field distribution of flat PET, structured PET, and structured PET with micron-sized scatters on the surface. The incident wavelength was set as 532 nm.

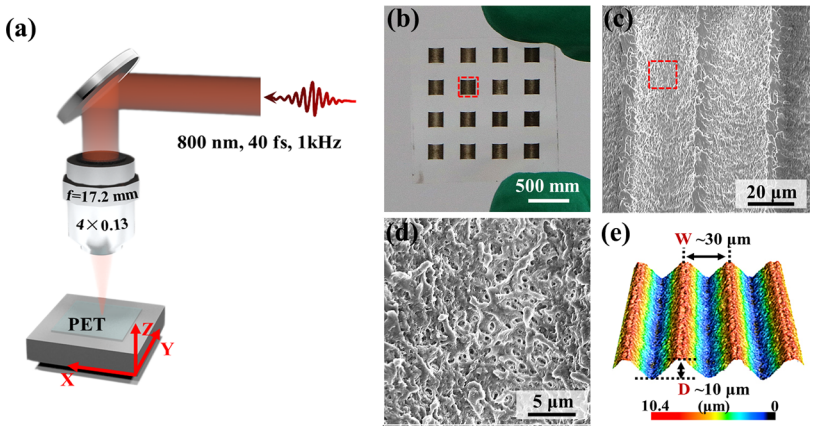

Figure 2. Morphology of the flexible PET substrate processed by the FsLDW technology. (a) Schematic experimental setup for the grating fabrication on the PET thin film. (b) Optical image of the large-area grating structure arrays. (c, d) SEM images of gratings with different magnifications. The random hierarchical micro/nanostructures are obvious. The red boxes in (b) and (c) represent only the approximate enlarged image area. (e) Three-dimensional (3D) confocal microscope image of the regular one-dimensional grating structures. The conditions with ~30 μm width and ~10 μm depth are displayed.

measured. Here, $\mu\varepsilon$ represents one-millionth of the strain of the sample, L denotes the original length of the cubic element in the sample, and ΔL represents the change in the length of the cubic element. A platform with four degrees of freedom was used to change the bending curvature of the substrates in steps of 0.25 mm. The data are recorded in real time with an analysis system (DongHua, DH5922N).

RESULT AND DISCUSSION

Near-Field Electric Field Calculation of the Structured PET. Figure 1a (top) shows a typical PET with grating structures. A micron-sized periodic sawtooth-shaped grating (30 μm in width and 10 μm in depth) is assumed, whose setting is to match the experimental parameters. For this type of structure, the optical diffraction in the far field has been mostly considered in previous studies, but here, we mainly focus on the near-field electric distribution caused by the structured surface. To illustrate this phenomenon, an FDTD method was employed for the simulation using Lumerical software. The RI values of the PET material corresponding to the different wavelengths in the visible range were taken from ref 45. The periodic conditions of the structure unit were applied on the left- and right-hand sides of the simulated domain. The mesh size (~20 nm) is set to be 1 order of magnitude smaller than the operating wavelength, which guarantees the convergence and the validity of the calculation results (Figure 1b).

As experienced in most transparent media, most of the incident light passes through the PET material. But for the structured one, the electric field distribution changes obviously (Figure 1b left and middle). Because the spatial periodicity of the sawtooth-shaped grating is much larger than the working wavelength (λ), there are hundreds of diffraction orders occurring according to the grating equation $d\sin\theta = N\lambda$ (θ is the incident angle), which leads to the strong interference of the electric field, especially in areas near the surface.[46] To further focus on the influence of the hierarchical micro/nanostructures on the electric field distribution, a layer of scatters with size smaller than 1 μm was randomly distributed on the structured PET surface. As a result, the diffraction lights were scattered around inside the material to result in the more complex and diffusion-like profile of the electric fields, as shown in Figure 1a (bottom) and Figure 1b (right). The surface with micro/nanomorphologies obviously enhances the light scattering and trapping, resulting in the local enhancement of the electric field in the near field. Interestingly, when we further simulated the electric field distribution of the substrates with different structural parameters, such an enhancement was found universal as long as the structural unit size of the sample is about an order of magnitude larger than the wavelength. This also suggests that there are no limitations in the specific dimension of the sample. Detailed simulation results can be found in Supporting Information (SI) Figure S1.

In addition to the influence mentioned above, we believe that there are two other factors that cannot be ignored: one is that the RI of PET (n_{PET}) is larger than that of air (n_{air}), which is likely to cause the total internal reflection at the interface and make the light localized inside the film.[10] The other is that the light

https://dx.doi.org/10.1021/acsami.0c04124
ACS Appl. Mater. Interfaces 2020, 12, 26614−26623

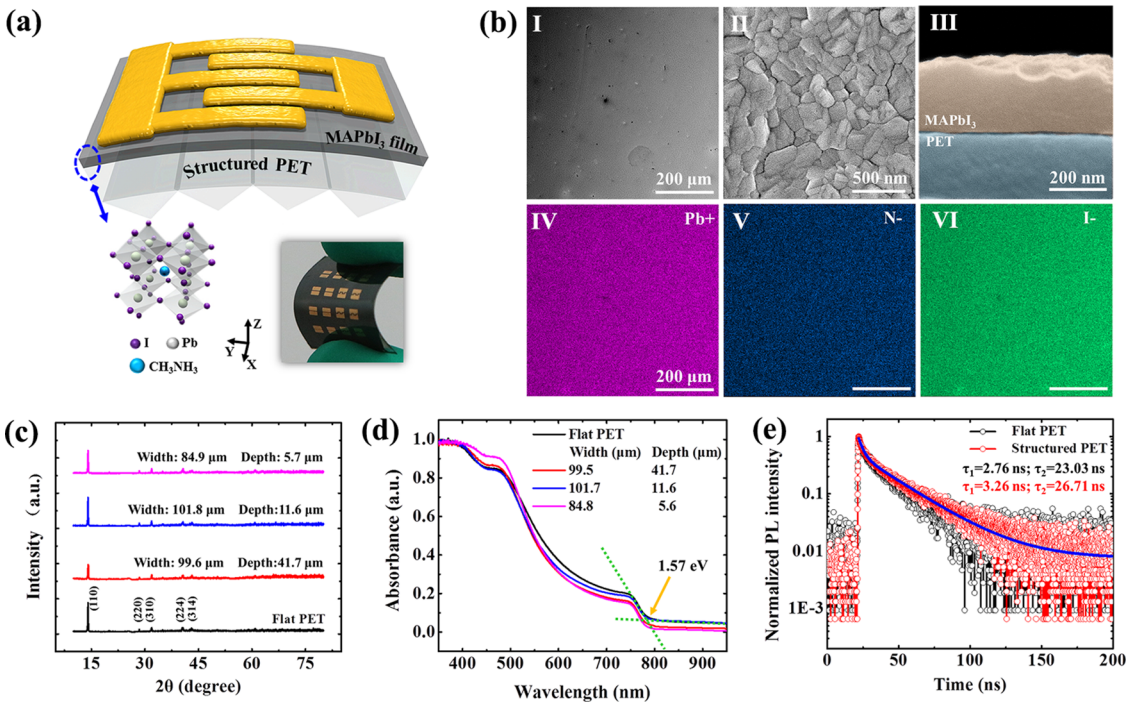

Figure 3. Performance characterization of the perovskite film. (a) Schematic device structure of the perovskite FPD. The top-down materials are gold electrodes, $MAPbI_3$ film, and structured PET substrate. The insets are the 3D schematic representation of $MAPbI_3$ (left) and the optical image of the flexible device (right). (b) SEM images (top) of $MAPbI_3$ material on top and cross-sectional views with different scale bars and the corresponding EDS images (bottom). The scanning areas of I, IV, V, and VI are the same. (c–e) XRD pattern, absorbance, and TRPL spectra comparison of $MAPbI_3$ film on different substrates. The processing parameters of the structured PET in (e) are 84.9 μm width and 5.7 μm depth. The properties of materials are almost unaffected by the substrate structures.

absorption coefficient of the PET is very low in the visible range, resulting in the multiple cycles of light transmission without losses. Therefore, the structured PET film not only acts as a supporter for perovskite materials but also participates in the light harvesting.

Micro/Nanostructures Fabrication on the Surface of PET Substrate. Figure 2a shows a schematic of processing micro/nanostructures on the surface of PET substrate using the FsLDW technology. A commercial chirped pulse amplification of the Ti:sapphire laser system served as the optical source, which delivers 1 kHz, 40 fs laser pulses with a central wavelength of 800 nm. An objective lens was used to spatially focus the laser beam onto the PET film, and the movement of the PET was controlled by a three-dimensional (3D) translation stage on which it was mounted. By adjusting the experimental conditions, such as energy, focal distance, and scanning velocity, grating with different widths and depths can be obtained flexibly on the PET film. Figure 2b exhibits several groups of the large-area grating structures, with coverage area of each being about 2 × 2 mm^2. The morphological details of the grating structures were characterized by a scanning electron microscope (SEM). After the laser processing, several hierarchical micro/nanostructures can be observed on the surface (Figure 2c,d). The 3D topography of the sawtooth-shaped surface structures with 30 μm width and 10 μm depth is observed with a confocal microscope image (Figure 2e). With different laser processing parameters, we also obtained the grating structures of other features. More details, including the processing parameters and the corresponding surface topographies, can be found in Supporting Information Figure S2.

Properties Characterization of Perovskite Film on Different Substrates. After the surface modification of PET, a $MAPbI_3$ film with a thickness of ∼200 nm was spin-coated on the flat surface using a one-step solution method.[47] The thickness of the film is suggested to be thin enough to reduce the lateral defects of the material, ensuring its in-plane uniformity and continuity. Then, several pairs of the interdigital electrodes (Au, 50 μm) were deposited on the film directly above the laser processing position. A typical planar metal–semiconductor–metal (MSM) model, being the so-called photoconductor type, was fabricated.[48] The schematic diagram and image of the device are shown in Figure 3a. This simple configuration facilitates our analysis of the device performance.[48] The morphology of the film was further characterized by the SEM images from the top and cross-sectional views (Figure 3b top). By controlling the nucleation rate and crystallization speed, a film with average grain size of ∼126 nm can completely cover the whole PET substrate (Supporting Information Figure S3). The energy-dispersive X-ray spectroscopy (EDS) of the film was measured (Figure 3b, bottom). The uniform elemental distribution of lead ($Pb2^+$), nitrogen (N^-), and iodine (I^-) indicates good crystalline quality, which facilitates the effective transport of photogenerated carriers, thereby resulting in outstanding device performance.

To explore the influence of the substrate on the material properties, the perovskites on the substrates with different processing parameters were characterized by X-ray diffraction (XRD), normalized degree of absorption (absorbance), and time-resolved photoluminescence (TRPL). The PET surface with violent structure morphology was chosen for comparison with the flat one. Figure 3c compares the measured XRD patterns of $MAPbI_3$ films on different substrates. No matter how the substrate changes in the surface morphology, we can still see the same peaks occurring at 14.05, 28.40, 31.90, 40.42, and

https://dx.doi.org/10.1021/acsami.0c04124
ACS Appl. Mater. Interfaces 2020, 12, 26614–26623

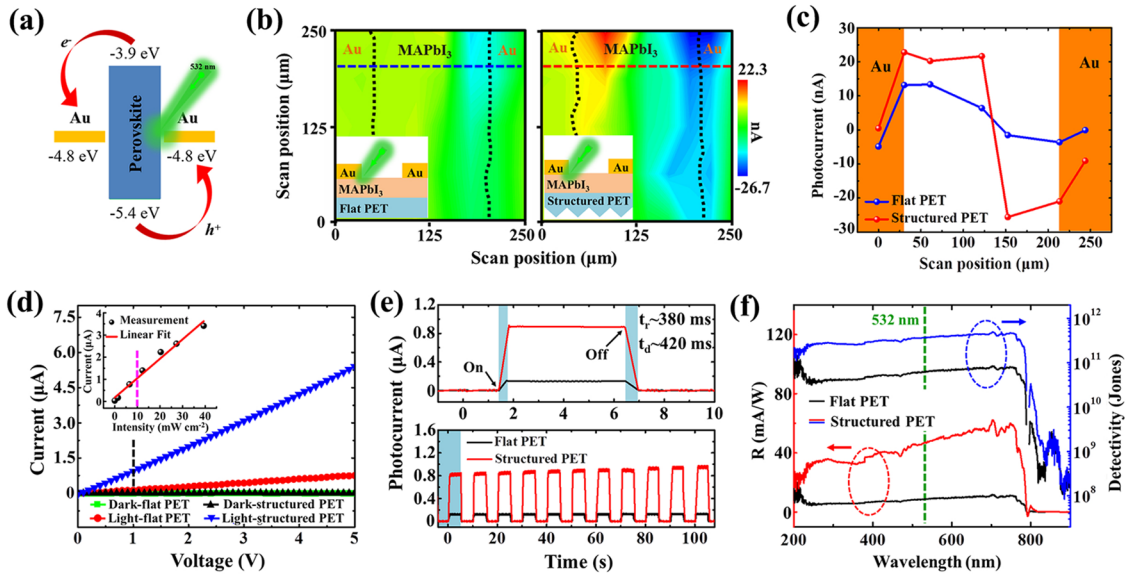

Figure 4. Photoresponse comparison of the $MAPbI_3$ perovskite FPD based on flat and structured substrates. (a) Energy diagram of perovskite-based MSM model. (b) SPI (main) and schematic diagram (inset) comparison of perovskite under zero bias and 532 nm laser excitation (100 mW cm^{-2}). The red and blue dotted lines are the scanning paths, which correspond to the scanning photocurrent measurements shown in (c). (d) Current−voltage plot of different devices under laser irradiation (10 mW cm^{-2}, 532 nm); inset: power-dependent photocurrent of perovskite on the structured substrate. The bias is fixed as 1 V. (e) Time-dependent photoresponse comparison. The rise time (t_r) and decay time (t_d) are defined as the time of 90% increase and decrease of the peak value, respectively. (f) Comparison of photoresponsivity (R) and detectivity (D^*) in the UV−NIR region.

43.03°, which correspond to the typical reflections of (110), (220), (310), (224), and (314) lattice planes. More detailed XRD information from 15 to 65° can be found in Supporting Information Figure S3. This indicates that there is no change in the lattice structure of the material. Similarly, regardless of variable structure parameters, a slope always appears at the position of ∼780 nm in the light absorption spectra, corresponding to the same band gap of ∼1.57 eV (Figure 3d). In the TRPL spectra, we can also see the almost identical two-exponential decay with a fast photocarrier lifetime of ∼3 ns and a slow one of ∼25 ns (Figure 3e). Further detailed experimental studies show that the structured substrate does contribute to the lifetime extension of its surface material (Supporting Information Figure S4). In contrast to our previous work, we believe that this similar phenomenon is due to the enhanced photon recycling and out-coupling effect caused by the structured substrate.[49] However, the change of PL lifetime (<5 ns) is not obvious, which also proves that the substrate has little effect on the radiative recombination process of the perovskite material. Therefore, we can conclude that the substrate with structures cannot change the properties of the materials, but only affect the light−matter interactions to enhance the utilization of the incident light. This design of the micro/nanostructured substrate possesses excellent compatibility and allows us to further improve the device performance as well as other excitation factors, such as making composition with nanowires (NW) or quantum dots (QD).[29,35,36]

Photoresponse Measurements of the Perovskite FPDs. After characterization of the perovskite film, we further measured the performance of the back-reflected photodetectors. Figure 4a presents its energy diagram, and a Schottky barrier develops at the interface between the gold electrodes and the $MAPbI_3$ film because of their different work functions, leading to a built-in electric field to restrain the free transportation of carriers and produce a small dark current without bias voltage and laser illumination.[50] However, this kind of equilibrium state can be easily broken under irradiation. The sample first absorbs photons and produces several photogenerated electron−hole pairs. Then, driven by the built-in field, the pairs begin to separate and the carrier density increases, which helps the carriers to participate in the current transport and enhances the current.[51] This process can be confirmed/clarified by scanning photocurrent imaging (SPI) experiments.[50] Figure 4b compares the SPI measurement results of the device with the structured and smooth substrates. The examination was performed under 532 nm irradiation of 100 mW cm^{-2} without an applied bias voltage. Obviously, two significant features can be observed: on the one hand, the strongest photoresponse with antisymmetric character occurs near the interface between the gold electrodes and the perovskite.[9,50] It illustrates the largest band offset due to the Schottky barrier located at the interface, which is the main location of generation and recombination of photogenerated carriers. The photovoltaic effect plays a crucial role here, and it has been widely confirmed in other photoelectric devices based on two-dimensional (2D) materials.[51−53] On the other hand, when we measured the photocurrent scanning along the MSM paths, as shown by the red and blue lines in Figure 4b,c, we found that the photoresponse of the structured device is stronger than that of the unstructured one. Due to the strong near-field electric field distribution caused by the structures of the back-reflected PET substrate, the light−mater interaction on the surface is enhanced, which in turn manifests as an increase in the EQE of the perovskite material.[17] Additional details are shown in Supporting Information Figure S5.

Afterward, the photoresponse of the device was measured under large bias voltages. Figure 4d compares the current of the perovskite on the flat and structured substrates without and with laser irradiation (532 nm, 10 mW cm^{-2}), respectively. Upon laser illumination, a typical linear current−voltage relationship could be observed with a higher than 5-fold increase of on/off ratio in the range of 0−5 V. The symmetrical MSM architecture suppressed the rectification and exhibited the Ohmic contact.[51]

https://dx.doi.org/10.1021/acsami.0c04124
ACS Appl. Mater. Interfaces 2020, 12, 26614−26623

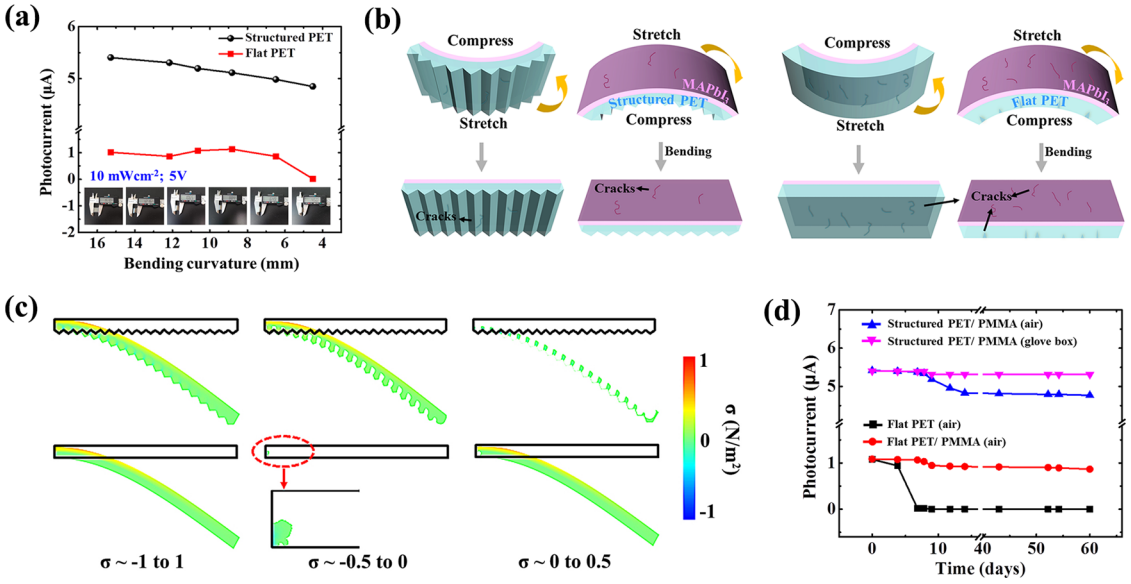

Figure 5. Bending stability measurements of the perovskite FPD. (a) Performance comparison of perovskite FPD on different substrates under different number of bending cycles and different curvature radii. Inset: Photographic images of the flexible operation. (b) Schematic of changes in device topography during bending. (c) Stress distribution simulation of PET substrates with and without micro/nanostructures under bending. (d) Stability comparison of different devices in 2 months.

This performance-enhanced photodetector presented a linear dependence of current on the power intensity from 0 to 40 mW cm^{-2} (Figure 4d, inset). However, with increasing power of the incident laser (>1500 mW cm^{-2}), the photoresponse of the FPD will be saturated. This is mainly because the strong incident light intensity continuously accumulates heat at the light spot area and causes irreversible defects and destructions to the perovskite material. Additional details are shown in Supporting Information Figure S6.

Then, we switched on and off the laser illumination on the sample, resulting in a periodically enhanced photocurrent (Figure 4e). Regardless of the structured and flat devices, the rise time (t_r) and decay time (t_d) are very similar, being about 380 and 420 ms, respectively. This means that our device cannot operate as a fast PD to respond effectively to pulsed incident light signals with frequency larger than 1.25 Hz. The response time is mainly limited by the material quality and the architecture of the devices. As a lateral photoconductor, our device exhibits a typical photoresponse time in the order of milliseconds (Table 1). We can further improve the response rate of our photodetector by optimizing the material quality or shortening the carrier transit length of the device.[48] Furthermore, we also compared two critical parameters of photoresponsivity (R) and detectivity (D^*) in a wide spectral range (200−1000 nm) for intuitive performance of the devices (Figure 4f), where a xenon lamp with a broad spectrum was used as the light source. We can find an enhancement of R and D^* with values of 47.1 mA W^{-1} and 3.7×10^{11} Jones, more than 5-fold enhancement at 532 nm. As the band gap of the $MAPbI_3$ perovskite material was measured as 1.57 eV, the sharp decreases in both R and D^* become obvious near the wavelength of 780 nm. This implies that our FPD has hardly any response to wavelengths above 790 nm. The fluctuation of D^* in the wavelength range of 800−1000 nm is derived by the light source performance, as shown in Supporting Information Figure S5.

The R value can be calculated according to the following formula

$$R = \Delta I/PS \quad (1)$$

where ΔI ($\Delta I = I_{light} - I_{dark}$) is the difference between the photocurrent and dark current, P is the incident light intensity.

The D^* value can be expressed by the following relationship if the shot noise from the dark current is the major contribution

$$D^* = R/\sqrt{2qJ_d} \quad (2)$$

where q is the absolute charge of electron and J_d ($J_d = I_d/S$) is the dark current density, and S is the effective illumination area.

A similar enhancement has also been observed in the back-reflected photodetectors with other processing conditions. The enhanced performance of devices under such structural design has proven to be universal. For details on the performance of other devices, see Supporting Information Figure S7. In addition, although the processed periodic sawtooth-shaped gratings on the substrate are unidirectional, there is no obvious photoelectric anisotropy of our devices because the characteristic size of the structures on the processed sample is much larger than the incident wavelength. For further detailed discussion, see Supporting Information Figure S8.

Mechanical Property Measurements of the Perovskite FPDs. The bending robustness of the structured flexible perovskite photodetector was characterized by monitoring the current alteration under a large number of bending cycles and different curvature radii. The initial dimension of the sample was 15.10 mm, and then it was bent to 12.16, 10.65, 8.84, 6.49, and 4.50 mm for respective 100 cycles. After a total of 500 bends, the photocurrent still maintained 89.8% of the initial value under 10 mW cm^{-2} laser irradiation (532 nm) and 1 V bias voltage actuation. The structured substrate is obviously beneficial for the maintenance of the device performance. Figure 5a shows the comparative results of the bending stability based on different substrates. When the flat substrate was bent to a radius of 4.51 mm, the photocurrent of the device reduced significantly. A large number of cracks were found on the surface of the perovskite material using a microscope. This indicates that, at this degree of bending, the material will be damaged by an increasing stress in

https://dx.doi.org/10.1021/acsami.0c04124
ACS Appl. Mater. Interfaces 2020, 12, 26614−26623

surface, thereby severely limiting the transportation of carriers driven by the electric field (Supporting Information Figure S9). As a comparison, we have not observed the similar rapid degradation in the structured devices. This phenomenon may stem from two reasons: First, since the specific area of the substrate is greatly increased after laser processing, the structure morphology is less likely to be destroyed after bending. Second, the overall stress distribution of the processed substrate also changed, which results in less fracture of the perovskite material.[54] Figure 5b presents the schematic of the device topography change for different substrates during bending. To verify the above deduction, we used finite-element method-based COMSOL Multiphysics software to simulate the stress distribution of the substrates under bending. It can be found that the micro/nanostructures on the structured substrate make the stress distribution more uniform inside the PET material, whereas the stress is more likely to be concentrated on the surface of the flat substrate (Figure 5c). This is the reason why the perovskite thin film on the flat substrate surface is more likely to be destroyed. Furthermore, we also carried out the microstrain ($\mu\varepsilon$) measurements of different PET samples. The $\mu\varepsilon$ value of the structured PET is found to be much smaller than that of the flat one, which directly indicates a relatively small stress on the structured PET surface under the same bending curvature. All of the results confirm that the micro/nanostructures on the substrate are beneficial to improve the bending robustness of the FPDs. The flexibility of PET has also been proved to be a key factor in determining the bending degree of our devices. More detailed illustration can be found in Supporting Information Figure S9.

Furthermore, the stability of the device was also evaluated and optimized. The organic−inorganic hybrid perovskite $MAPbI_3$ presents poor long-term stability because of the impact of defects and ion migration, which greatly limits its practical applications.[55,56] To maintain the stability of related devices, the environment with low temperature and humidity (<85 °C and 30%) is required.[56] In our experiment, we first placed an FPD base on the unprocessed substrate without surface protection in air when the average temperature and humidity are 25 °C and 15%, respectively. It was found that the stability of this device was only maintained for about 4 days before its photocurrent greatly reduced (Figure 5d). To avoid degradation, the PMMA encapsulation technology was applied for both samples respectively with processed and unprocessed substrates.[57] When the reference samples protected in the nitrogen atmosphere (H_2O < 0.1 ppm, O_2 < 0.1 ppm) were compared, we can find that 88% of the excellent performance almost maintained for more than 2 months. The protection effect of the devices is similar to the results reported in other studies.[57]

CONCLUSIONS

In conclusion, by fabricating the periodic micron-sized grating structures on the surface of PET using the FsLDW technology, we have demonstrated a facile and effective design for near-field optical enhancement in this flexible material. The simulation of the electric field distribution shows that the hierarchical micro/nanostructures on the surface play a crucial role in this phenomenon. Then, by adopting it as a back-reflected substrate, we designed a flexible and performance-enhancing $MAPbI_3$ perovskite photodetector. Further experimental characterizations indicate that the structural design of the $MAPbI_3$ film is likely to enhance the light−matter interaction without a change in the material properties, leading to an at least 5-fold performance enhancement in photoresponsivity, detectivity, and on/off ratio without deterioration in the photoresponse speed. In addition, our flexible perovskite photodetector also exhibits excellent robustness even under a small curvature radius (4.51 mm) even after 500 bending cycles. Combined with PMMA encapsulation, the performance of the devices can maintain nearly 90% in 2 months in air. Our work highlights the positive effects of the structured substrate on the device performance. Thanks to the relative maturity of membrane-forming and femtosecond laser processing technologies, our structural design has potential for practical applications because of the enhanced optoelectronic and mechanical properties.

ASSOCIATED CONTENT

Supporting Information

The Supporting Information is available free of charge at https://pubs.acs.org/doi/10.1021/acsami.0c04124.

Simulated near-field electric field distribution of PETs with and without structures under light illumination at different wavelengths, the former of which possess different grating morphologies with and without micron-sized scatters on the surface; processing parameters and the corresponding morphologies of grating structures; EQE comparison of perovskite photodetectors with different substrates; photoresponse measurement of another back-reflected FPD; and FPD bending performance comparison of devices with different substrates (PDF)

AUTHOR INFORMATION

Corresponding Authors

Wei Xin − *State Key Laboratory for Applied Optics, Changchun Institute of Optics, Fine Mechanics and Physics, Chinese Academy of Sciences, Changchun 130033, China;* orcid.org/0000-0002-1887-7535; Email: weixin@ciomp.ac.cn

Shuqi Chen − *The Key Laboratory of Weak Light Nonlinear Photonics Ministry of Education, Teda Applied Physics Institute and School of Physics, Nankai University, Tianjin 300071, China;* orcid.org/0000-0002-7898-4148; Email: schen@nankai.edu.cn

Jianjun Yang − *State Key Laboratory for Applied Optics, Changchun Institute of Optics, Fine Mechanics and Physics, Chinese Academy of Sciences, Changchun 130033, China;* Email: jjyang@ciomp.ac.cn

Chunlei Guo − *State Key Laboratory for Applied Optics, Changchun Institute of Optics, Fine Mechanics and Physics, Chinese Academy of Sciences, Changchun 130033, China; The Institute of Optics, University of Rochester, Rochester, New York 14627, United States;* orcid.org/0000-0001-8525-6301; Email: guo@optics.rochester.edu

Authors

Ye Wang − *State Key Laboratory for Applied Optics, Changchun Institute of Optics, Fine Mechanics and Physics, Chinese Academy of Sciences, Changchun 130033, China; Center of Materials Science and Optoelectronics Engineering, University of Chinese Academy of Sciences, Beijing 100049, China*

Wenwei Liu − *The Key Laboratory of Weak Light Nonlinear Photonics Ministry of Education, Teda Applied Physics Institute and School of Physics, Nankai University, Tianjin 300071, China*

Tingting Zou − *State Key Laboratory for Applied Optics, Changchun Institute of Optics, Fine Mechanics and Physics,*

https://dx.doi.org/10.1021/acsami.0c04124
ACS Appl. Mater. Interfaces 2020, 12, 26614−26623

Chinese Academy of Sciences, Changchun 130033, China; Center of Materials Science and Optoelectronics Engineering, University of Chinese Academy of Sciences, Beijing 100049, China

Xin Zheng − *State Key Laboratory for Applied Optics, Changchun Institute of Optics, Fine Mechanics and Physics, Chinese Academy of Sciences, Changchun 130033, China; Center of Materials Science and Optoelectronics Engineering, University of Chinese Academy of Sciences, Beijing 100049, China*

Yanshuang Li − *Center of Materials Science and Optoelectronics Engineering, University of Chinese Academy of Sciences, Beijing 100049, China; State Key Laboratory of Luminescence and Applications, Changchun Institute of Optics, Fine Mechanics and Physics, Chinese Academy of Sciences, Changchun 130033, China*

Xiuhua Xie − *State Key Laboratory of Luminescence and Applications, Changchun Institute of Optics, Fine Mechanics and Physics, Chinese Academy of Sciences, Changchun 130033, China*

Xiaojuan Sun − *State Key Laboratory of Luminescence and Applications, Changchun Institute of Optics, Fine Mechanics and Physics, Chinese Academy of Sciences, Changchun 130033, China*

Weili Yu − *State Key Laboratory for Applied Optics, Changchun Institute of Optics, Fine Mechanics and Physics, Chinese Academy of Sciences, Changchun 130033, China;* orcid.org/0000-0001-5075-9638

Zhibo Liu − *The Key Laboratory of Weak Light Nonlinear Photonics Ministry of Education, Teda Applied Physics Institute and School of Physics, Nankai University, Tianjin 300071, China;* orcid.org/0000-0001-9210-156X

Complete contact information is available at: https://pubs.acs.org/10.1021/acsami.0c04124

Author Contributions

The manuscript was written through contributions of all authors. All authors have given approval to the final version of the manuscript.

Notes

The authors declare no competing financial interest.

■ ACKNOWLEDGMENTS

This study was financially supported by the K. C. Wong Education Foundation (GJTD-2018-08), National Natural Science Foundation of China (grant nos. 91750205, 11804334, and 11674178), Jilin Provincial Science & Technology Development Project (20180414019GH), and Natural Science Foundation of Tianjin City (17JCZDJC37900).

■ ABBREVIATIONS

FPDs, flexible photodetectors
FsLDW, femtosecond laser direct writing
FDTD, finite-difference time-domain
SPI, scanning photocurrent imaging
RI, refractive index
$MAPbI_3$, $CH_3NH_3PbI_3$
PET, poly(ethylene terephthalate)
PMMA, poly(methyl methacrylate)
DMF, *N*,*N*-dimethylformamide
DMSO, dimethyl sulfoxide

■ REFERENCES

(1) Han, S. T.; Peng, H.; Sun, Q.; Venkatesh, S.; Chung, K. S.; Lau, S. C.; Zhou, Y.; Roy, V. A. L. An Overview of the Development of Flexible Sensors. *Adv. Mater.* **2017**, *29*, No. 1700375.

(2) Kamyshny, A.; Magdassi, S. Conductive Nanomaterials for 2D and 3D Printed Flexible Electronics. *Chem. Soc. Rev.* **2019**, *48*, 1712−1740.

(3) Britnell, L.; Ribeiro, R. M.; Eckmann, A.; Jalil, R.; Belle, B. D.; Mishchenko, A.; Kim, Y.-J.; Gorbachev, R. V.; Georgiou, T.; Morozov, S. V.; Grigorenko, A. N.; Geim, A. K.; Casiraghi, C.; Castro Neto, A. H.; Novoselov, K. S. Strong Light-Matter Interactions In Heterostructures of Atomically Thin Films. *Science* **2013**, *340*, 1311−1314.

(4) You, R.; Liu, Y. Q.; Hao, Y. L.; Han, D. D.; Zhang, Y. L.; You, Z. Laser Fabrication of Graphene-Based Flexible Electronics. *Adv. Mater.* **2020**, *32*, No. 1901981.

(5) Dong, Q.; Fang, Y.; Shao, Y.; Mulligan, P.; Qiu, J.; Cao, L.; Huang, J. Electron-Hole Diffusion Lengths > 175 μm in Solution-Grown CH3NH3PbI3 Single Crystals. *Science* **2015**, *347*, 967−970.

(6) Konstantatos, G.; Badioli, M.; Gaudreau, L.; Osmond, J.; Bernechea, M.; Pelayo Garcia de Arquer, F.; Gatti, F.; Koppens, F. H. L. Hybrid Graphene-Quantum Dot Phototransistors with Ultrahigh Gain. *Nat. Nanotechnol.* **2012**, *7*, 363−368.

(7) Furchi, M.; Urich, A.; Pospischil, A.; Lilley, G.; Unterrainer, K.; Detz, H.; Klang, P.; Andrews, A. M.; Schrenk, W.; Strasser, G.; Mueller, T. Microcavity-Integrated Graphene Photodetector. *Nano Lett.* **2012**, *12*, 2773−2777.

(8) Echtermeyer, T. J.; Britnell, L.; Jasnos, P. K.; Lombardo, A.; Gorbachev, R. V.; Grigorenko, A. N.; Geim, A. K.; Ferrari, A. C.; Novoselov, K. S. Strong Plasmonic Enhancement of Photovoltage in Graphene. *Nat. Commun.* **2011**, *2*, No. 458.

(9) Xin, W.; Chen, X. D.; Liu, Z. B.; Jiang, W. S.; Gao, X. G.; Jiang, X. Q.; Chen, Y.; Tian, J. G. Photovoltage Enhancement in Twisted-Bilayer Graphene Using Surface Plasmon Resonance. *Adv. Opt. Mater.* **2016**, *4*, 1703−1710.

(10) Saxena, K.; Jain, V.; Singh Mehta, D. A Review on the Light Extraction Techniques in Organic Electroluminescent Devices. *Opt. Mater.* **2009**, *32*, 221−233.

(11) Feng, J.; Liu, Y.; Bi, Y.; Sun, H. Light Manipulation in Organic Light-Emitting Devices by Integrating Micro/Nano Patterns. *Laser Photonics Rev.* **2017**, *11*, No. 1600145.

(12) Wang, W.; Qi, L. Light Management with Patterned Micro- and Nanostructure Arrays for Photocatalysis, Photovoltaics, and Optoelectronic and Optical Devices. *Adv. Funct. Mater.* **2019**, *29*, No. 1807275.

(13) Vorobyev, A.; Guo, C. Direct Femtosecond Laser Surface Nano/Microstructuring and its Applications. *Laser Photonics Rev.* **2013**, *7*, 385−407.

(14) Jiang, L.; Wang, A.; Li, B.; Cui, T.; Lu, Y. Electrons Dynamics Control by Shaping Femtosecond Laser Pulses in Micro/Nanofabrication: Modeling, Method, Measurement and Application. *Light: Sci. Appl.* **2018**, *7*, No. 17134.

(15) *Lumerical FDTD Solutions*; LumericalSolutions, Inc. http://www.lumerical.com/tcad-products/fdtd/ 2014.

(16) Yu, Z.; Raman, A.; Fan, S. Fundamental Limit of Nanophotonic Light Trapping in Solar Cells. *Proc. Natl. Acad. Sci. U.S.A.* **2010**, *107*, 17491−17496.

(17) Kelzenberg, M.; Boettcher, S.; Petykiewicz, J.; Turner-Evans, D.; Putnam, M.; Warren, E.; Spurgeon, J.; Briggs, R.; Lewis, N.; Atwater, H. Enhanced Absorption and Carrier Collection in Si Wire Arrays for Photovoltaic Applications. *Nat. Mater.* **2010**, *9*, 239−244.

(18) Zhang, Y. P.; Lim, C. K.; Dai, Z. G.; Yu, D. N.; Haus, J. W.; Zhang, H.; Prasad, P. N. Photonics and Optoelectronics Using Nano-Structured Hybrid Perovskite Media and their Optical Cavities. *Phys. Rep.* **2019**, *795*, 1−51.

(19) Qi, X.; Zhang, Y.; Ou, Q.; Ha, S.; Qiu, C.; Zhang, H.; Cheng, Y.; Xiong, Q.; Bao, Q. Photonics and Optoelectronics of 2D Metal-Halide Perovskites. *Small* **2018**, *14*, No. 1800682.

(20) National Renewable Energy Laboratory, Best Research-Cell Efficiencies Chart. http://www.nrel.gov/pv/ (accessed Aug, 2019).

(21) Valverde-Chávez, D. A.; Ponseca, C. S.; Stoumpos, C. C.; Yartsev, A.; Kanatzidis, M. G.; Sundström, V.; Cooke, D. G. Intrinsic femtosecond charge generation dynamics in single crystal CH3NH3PbI3. *Energy Environ. Sci.* **2015**, *8*, 3700−3707.

(22) Miyata, A.; Mitioglu, A.; Plochocka, P.; Portugall, O.; Wang, J. T. W.; Stranks, S. D.; Snaith, H. J.; Nicholas, R. J. Direct measurement of

the exciton binding energy and effective masses for charge carriers in organic−inorganic tri-halide perovskites. *Nat. Phys.* **2015**, *11*, 582−587.
(23) Li, P.; Chen, Y.; Yang, T.; Wang, Z.; Lin, H.; Xu, Y.; Li, L.; Mu, H.; Shivananju, B.; Zhang, Y.; Zhang, Q.; Pan, A.; Li, S.; Tang, D.; Jia, B.; Zhang, H.; Bao, Q. Two-Dimensional $CH_3NH_3PbI_3$ Perovskite Nanosheets for Ultrafast Pulsed Fiber Lasers. *ACS Appl. Mater. Interfaces* **2017**, *9*, 12759.
(24) Hu, X.; Zhang, X.; Liang, L.; Bao, J.; Li, S.; Yang, W.; Xie, Y. High-Performance Flexible Broadband Photodetector Based on Organolead Halide Perovskite. *Adv. Funct. Mater.* **2014**, *24*, 7373−7380.
(25) Cheng, Y.; Shi, Z.; Yin, S.; Li, Y.; Li, S.; Liang, W.; Wu, D.; Tian, Y.; Li, X. Photovoltaic Broadband Photodetectors Based on $CH_3NH_3PbI_3$ Thin Films Grown on Silicon Nanoporous Pillar Array. *Sol. Energy Mater. Sol. Cells* **2020**, *204*, No. 110230.
(26) Tan, Q.; Ye, G.; Zhang, Y.; Du, X.; Liu, H.; Xie, L.; Zhou, Y.; Liu, N. Vacuum-Filtration Enabled Large-Area $CsPbBr_3$ Films on Porous Substrates for Flexible Photodetectors. *J. Mater. Chem. C* **2019**, *7*, 13402−13409.
(27) Richter, J.; Abdi-Jalebi, M.; Sadhanala, A.; Tabachnyk, M.; Rivett, J.; Pazos-Outo′n, L.; Gödel, K.; Price, M.; Deschler, F.; Friend, R. Enhancing Photoluminescence Yields in Lead Halide Perovskites by Photon Recycling and Light Out-Coupling. *Nat. Commun.* **2016**, *7*, No. 13941.
(28) Hu, W.; Huang, W.; Yang, S.; Wang, X.; Jiang, Z.; Zhu, X.; Zhou, H.; Liu, H.; Zhang, Q.; Zhuang, X.; Yang, J.; Kim, D.; Pan, A. High-Performance Flexible Photodetectors Based on High-Quality Perovskite Thin Films by a Vapor-Solution Method. *Adv. Mater.* **2017**, *29*, No. 1703256.
(29) Lee, Y.; Kwon, J.; Hwang, E.; Ra, C.; Yoo, W.; Ahn, J.; Hyeok Park, J.; Ho Cho, J. High-Performance Perovskite-Graphene Hybrid Photodetector. *Adv. Mater.* **2015**, *27*, 41−46.
(30) Ma, C.; Shi, Y.; Hu, W.; Chiu, M.; Liu, Z.; Bera, A.; Li, F.; Wang, H.; Li, L.; Wu, T. Heterostructured $WS_2/CH_3NH_3PbI_3$ Photoconductors with Suppressed Dark Current and Enhanced Photodetectivity. *Adv. Mater.* **2016**, *28*, 3683−3689.
(31) Gao, T.; Zhang, Q.; Chen, J.; Xiong, X.; Zhai, T. Performance-Enhancing Broadband and Flexible Photodetectors Based on Perovskite/ZnO-Nanowire Hybrid Structures. *Adv. Opt. Mater.* **2017**, *5*, No. 1700206.
(32) Wang, Y.; Zhang, Y.; Lu, Y.; Xu, W.; Mu, H.; Chen, C.; Qiao, H.; Song, J.; Li, S.; Sun, B.; Cheng, Y.; Bao, Q. Hybrid Graphene-Perovskite Phototransistors with Ultrahigh Responsivity and Gain. *Adv. Opt. Mater.* **2015**, *3*, 1389−1396.
(33) Sun, Z.; Aigouy, L.; Chen, Z. Plasmonic-Enhanced Perovskite-Graphene Hybrid Photodetectors. *Nanoscale* **2016**, *8*, 7377−7383.
(34) Luo, X.; Zhao, F.; Liang, Y.; Du, L.; Lv, W.; Xu, K.; Wang, Y.; Peng, Y. Facile Nanogold-Perovskite Enabling Ultrasensitive Flexible Broadband Photodetector with pW Scale Detection Limit. *Adv. Opt. Mater.* **2018**, *6*, No. 1800996.
(35) He, M.; Chen, Y.; Liu, H.; Wang, J.; Fang, X.; Liang, Z. Chemical Decoration of $CH_3NH_3PbI_3$ Perovskites with Graphene Oxides for Photodetector Applications. *Chem. Commun.* **2015**, *51*, 9659−9661.
(36) Cao, F.; Tian, W.; Gu, B.; Ma, Y.; Lu, H.; Li, L. High-Performance UV−vis Photodetectors Based on Electrospun ZnO Nanofiber-Solution Processed Perovskite Hybrid Structures. *Nano Res.* **2017**, *10*, 2244−2256.
(37) Xia, H.; Tong, S.; Zhang, C.; Wang, C.; Sun, J.; He, J.; Zhang, J.; Gao, Y.; Yang, J. Flexible and Air-stable Perovskite Network Photodetectors Based on $CH_3NH_3PbI_3$/C8BTBT Bulk Heterojunction. *Appl. Phys. Lett.* **2018**, *112*, No. 233301.
(38) Li, J.; Shen, Y.; Liu, Y.; Shi, F.; Ren, X.; Niu, T.; Zhao, K.; Liu, S. Stable High-Performance Flexible Photodetector Based on Upconversion Nanoparticles/Perovskite Microarrays Composite. *ACS Appl. Mater. Interfaces* **2017**, *9*, 19176−19183.
(39) Chen, S.; Teng, C.; Zhang, M.; Li, Y.; Xie, D.; Shi, G. A Flexible UV-Vis-NIR Photodetector Based on a Perovskite/Conjugated-Polymer Composite. *Adv. Mater.* **2016**, *28*, 5969.
(40) Liu, J.; Xue, Y.; Wang, Z.; Xu, Z.; Zheng, C.; Weber, B.; Song, J.; Wang, Y.; Lu, Y.; Zhang, Y.; Bao, Q. Two-Dimensional $CH_3NH_3PbI_3$ Perovskite: Synthesis and Optoelectronic Application. *ACS Nano* **2016**, *10*, 3536−3542.
(41) Zhu, P.; Gu, S.; Shen, X.; Xu, N.; Tan, Y.; Zhuang, S.; Deng, Y.; Lu, Z.; Wang, Z.; Zhu, J. Direct Conversion of Perovskite Thin Films into Nanowires with Kinetic Control for Flexible Optoelectronic Devices. *Nano Lett.* **2016**, *16*, 871−876.
(42) Li, J.; Liu, Y.; Ren, X.; Yang, Z.; Li, R.; Su, H.; Yang, X.; Xu, J.; Xu, H.; Hu, J.; Amassian, A.; Zhao, K.; Liu, S. F. Solution Coating of Superior Large-area Flexible Perovskite Thin Films with Controlled Crystal Packing. *Adv. Opt. Mater.* **2017**, *5*, No. 1700102.
(43) Zhu, B.; He, Z.; Yao, J.; Chen, C.; Wang, K.; Yao, H.; Liu, J.; Yu, S. Potassium Ion Assisted Synthesis of Organic-Inorganic Hybrid Perovskite Nanobelts for Stable and Flexible Photodetectors. *Adv. Opt. Mater.* **2018**, *6*, No. 1701029.
(44) Du, B.; Yang, W.; Jiang, Q.; Shan, H.; Luo, D.; Li, B.; Tang, W.; Lin, F.; Shen, B.; Gong, Q.; Zhu, X.; Zhu, R.; Fang, Z. Plasmonic-Functionalized Broadband Perovskite Photodetector. *Adv. Opt. Mater.* **2018**, *6*, No. 1701271.
(45) Iiyama, K.; Ishida, T.; Ono, Y.; Maruyama, T.; Yamagishi, T. Fabrication and Characterization of Amorphous Polyethylene Terephthalate Optical Waveguides. *IEEE Photonics Technol. Lett.* **2011**, *23*, 275−277.
(46) Liu, W.; Li, Z.; Cheng, H.; Chen, S.; Tian, J. Momentum Analysis for Metasurfaces. *Phys. Rev. Appl.* **2017**, *8*, No. 014012.
(47) Wang, Y.; Song, Q.; Lin, T.; Fu, Y.; Sun, X.; Chu, B.; Jin, F.; Zhao, H.; Li, W.; Su, Z.; Li, Y. Improved Performance of $CH_3NH_3PbI_3$ based Photodetector with a MoO_3 Interface Layer. *Org. Electron.* **2017**, *49*, 355−359.
(48) Wang, H.; Kim, D. Perovskite-Based Photodetectors: Materials and Devices. *Chem. Soc. Rev.* **2017**, *46*, 5204−5236.
(49) Xing, J.; Zheng, X.; Yu, Z.; Lei, Y.; Hou, L.; Zou, Y.; Zhao, C.; Wang, B.; Yu, H.; Pan, D.; Zhai, Y.; Cheng, J.; Zhou, D.; Qu, S.; Yang, J.; Ganeev, R. A.; Yu, W.; Guo, C. Dramatically Enhanced Photoluminescence from Femtosecond Laser Induced Micro-/Nanostructures on $MAPbBr_3$ Single Crystal Surface. *Adv. Opt. Mater.* **2018**, *6*, No. 1800411.
(50) Mueller, T.; Xia, F.; Freitag, M.; Tsang, J.; Avouris, P. Role of Contacts in Graphene Transistors: A Scanning Photocurrent Study. *Phys. Rev. B* **2009**, *79*, No. 245430.
(51) Xin, W.; Jiang, H.; Li, X.; Zhou, X.; Lu, J.; Yang, J.; Guo, C.; Liu, Z.; Tian, J. Photoinduced Orientation-Dependent Interlayer Carrier Transportation in Cross-Stacked Black Phosphorus Van Der Waals Junctions. *Adv. Mater. Interfaces* **2018**, *5*, No. 1800964.
(52) Koppens, F.; Mueller, T.; Avouris, Ph.; Ferrari, A.; Vitiello, M.; Polini, M. Photodetectors based on Graphene, other Two-Dimensional Materials and Hybrid Systems. *Nat. Nanotechnol.* **2014**, *9*, 780−793.
(53) Xin, W.; Li, X.; He, X.; Su, B.; Jiang, X.; Huang, K.; Zhou, X.; Liu, Z.; Tian, J. Black-Phosphorus-based Orientation-Induced Diodes. *Adv. Mater.* **2018**, *30*, No. 1704653.
(54) Lim, M.; Kim, D.; Park, C.; Lee, Y.; Han, S.; Li, Z.; Williams, R.; Park, I. A New Route toward Ultrasensitive, Flexible Chemical Sensors: Metal Nanotubes by Wet-Chemical Synthesis along Sacrificial Nanowire Templates. *ACS Nano* **2012**, *6*, 598−608.
(55) Chen, K.; Zhong, Q. H.; Chen, W.; Sang, B. H.; Wang, Y. W.; Yang, T. Q.; Liu, Y. L.; Zhang, Y. P.; Zhang, H. Short-Chain Ligand-Passivated Stable α-$CsPbI_3$ Quantum Dot for All-Inorganic Perovskite Solar Cells. *Adv. Funct. Mater.* **2019**, *29*, No. 1900991.
(56) Chen, B.; Rudd, P. N.; Yang, S.; YuanY, B.; Huang, J. S. Imperfections and their passivation in halide perovskite solar cells. *Chem. Soc. Rev.* **2019**, *48*, 3842.
(57) Asuo, I. M.; Fourmont, P.; Ka, I.; Gedamu, D.; Bouzidi, S.; Pignolet, A.; Nechache, R.; Cloutier, S. G. Highly efficient and ultrasensitive large-area flexible photodetector based on perovskite nanowires. *Small* **2019**, *15*, No. 1804150.

https://dx.doi.org/10.1021/acsami.0c04124
ACS Appl. Mater. Interfaces 2020, 12, 26614−26623